

Solution Structure of Heavy Meromyosin by Small-angle Scattering*

Received for publication, October 15, 2002, and in revised form, December 3, 2002
Published, JBC Papers in Press, December 3, 2002, DOI 10.1074/jbc.M210558200

Samantha P. Harris^{‡§}, William T. Heller[¶], Marion L. Greaser[¶], Richard L. Moss[‡],
and Jill Trehwella[¶]

From the [‡]Department of Physiology, University of Wisconsin Medical School, Madison, Wisconsin 53706,
[¶]Bioscience Division, Los Alamos National Laboratory, Los Alamos, New Mexico 87545,
and [§]Meat Science and Muscle Biology Laboratory, University of Wisconsin, Madison, Wisconsin 53706

Elucidation of x-ray crystal structures for the S1 subfragment of myosin afforded atomic resolution of the nucleotide and actin binding sites of the enzyme. The structures have led to more detailed hypotheses regarding the mechanisms by which force generation is coupled to ATP hydrolysis. However, the three-dimensional structure of double-headed myosin consisting of two S1 subfragments has not yet been solved. Therefore, to investigate the overall shape and relative orientations of the two heads of myosin, we performed small-angle x-ray and neutron scattering measurements of heavy meromyosin containing all three light chains (LC₁₋₃) in solution. The resulting small-angle scattering intensity profiles were best fit by models of the heavy meromyosin head-tail junction in which the angular separation between heads was less than 180 degrees. The S1 heads of the best fit models are not related by an axis of symmetry, and one of the two S1 heads is bent back along the rod. These results provide new information on the structure of the head-tail junction of myosin and indicate that combining scattering measurements with high resolution structural modeling is a feasible approach for investigating myosin head-head interactions in solution.

Myosin II, the major contractile protein of muscle, consists of two globular catalytic domains, referred to as S1 subfragments, attached to a long coiled-coil rod. Insights into the mechanisms of contraction were provided by x-ray crystal structures of individual S1 fragments from several myosin isoforms (1–3). From these studies it is now apparent that each S1 can be divided into two subdomains; that is, a globular motor domain that contains separate actin and nucleotide binding sites and an unusual ~8.5-nm α -helical segment, the so-called light chain binding domain, which connects the motor domain to the coiled-coil rod. ATP hydrolysis at the catalytic domain is thought to result in an angular rotation of the light chain binding domain that corresponds to the force-generating “power stroke” of the catalytic cycle of the enzyme (4).

* This work was performed under the auspices of the U. S. Department of Energy (DOE) (Contract W-7410-ENG036) and was supported by the DOE Biological and Environmental Research Project KP1101010 (to J. T.) in support of the Oak Ridge National Laboratory Structural Molecular Biology Program and by National Institutes of Health (NIH) Grant P01-HL47053 (to R. L. M.), a grant from the United States Department of Agriculture (to M. L. G.), and NIH National Research Service Award HL10161-02 (to S. P. H.). The costs of publication of this article were defrayed in part by the payment of page charges. This article must therefore be hereby marked “advertisement” in accordance with 18 U.S.C. Section 1734 solely to indicate this fact.

§ To whom correspondence should be addressed: 109 SMI, 1300 University Ave., Madison, WI 53706. Tel.: 608-262-7586; Fax: 608-265-5512; E-mail: spharris@physiology.wisc.edu.

Despite recent progress toward understanding the molecular basis of force generation, significant questions regarding the structure and function of myosin remain. In particular, since a high resolution structure for a two-headed myosin molecule is not yet available, comparatively little is known regarding potential head-head interactions or the arrangement at the S1/S2 junction, *i.e.* the region where each S1 domain joins the proximal (S2) section of the myosin rod. In smooth and invertebrate myosins, activation of ATPase activity is dependent on events occurring at this junction, such as Ca²⁺ binding or phosphorylation of the regulatory light chains, accessory proteins that bind the light chain binding domain near the S1/S2 junction. For these regulated myosins, activation appears to involve a significant conformational change that encompasses both head-head and head-tail interactions (5). By contrast, activation of unregulated myosins such as those of skeletal and cardiac muscle occurs primarily through events related to Ca²⁺ binding to the thin filament. Nonetheless, characteristics of the S1/S2 junction such as flexibility and angle of S1 attachment are still expected to have significant effects on the magnitude and rate of force generation. Consistent with this, regulatory light chain phosphorylation potentiates force and the rate of force development in skeletal muscle fibers (6).

Steric constraints or cooperative interactions between heads may also affect motor function in unregulated myosins. For instance, steric hindrance between the heads may result in nonequivalent actin binding affinities, potentially leading to cooperative binding (7, 8). Similarly, cooperativity was implied by single molecule force and displacement measurements that indicated both heads are necessary for maximum force generation by myosin (9). However, because spectroscopic (10) and electron micrograph studies (11, 12) suggest the S1/S2 junction is quite flexible, a structural basis for head-head interactions has been difficult to resolve.

In this paper, we present low resolution structural data on the overall conformation of myosin in solution. Small-angle x-ray and neutron scattering experiments were performed on heavy meromyosin (HMM),¹ a soluble proteolytic fragment of myosin. Neutron scattering measurements were used to obtain structural information regarding the longest particle dimensions of HMM that were necessary to accurately describe and model the molecule. X-ray scattering measurements were used for comparison to confirm overall HMM configuration as well as to check for monodispersity in solution and assure there were no concentration-dependent interparticle interference effects that would bias the modeling. Comparisons of the neutron scattering intensity profiles with simulated spectra generated from an existing model of the head-tail junction of myosin (13) indicated that the model may not accurately represent the

¹ The abbreviation used is: HMM, heavy meromyosin.

structure of HMM in solution. Instead, experimental small-angle scattering intensity profiles were reproduced by simple models in which the S1 heads were joined asymmetrically to a coiled-coil rod.

MATERIALS AND METHODS

Sample Preparation—Myosin was purified from rabbit back and leg fast twitch skeletal muscle according to Wagner and Giniger (14). HMM was prepared by limited α -chymotryptic digestion of myosin according to Weeds and Pope (15). To minimize degradation of regulatory light chain, myosin was digested in the presence of 2 mM MgCl_2 at a myosin:chymotrypsin ratio of 400:1 for 6 min at 22 °C. After precipitation of rod fragments and undigested myosin in 1 mM EDTA and 1 mM dithiothreitol, HMM in the supernatant was dialyzed against 50 mM Tris-Cl, pH 7.2, and further fractionated by fast protein liquid chromatography over a Q-Sepharose ion exchange column. Peak fractions were pooled, mixed with an equal volume of glycerol, and stored at -20 °C before use (within 14 days) in scattering experiments.

For x-ray scattering measurements, purified HMM was dialyzed extensively against experimental buffers containing 150 mM KCl, 20 mM imidazole, pH 7.0, 1 mM EDTA, and 1 mM dithiothreitol. Solutions of similar composition were used for neutron scattering experiments, except that D_2O was used in place of H_2O to increase scattering signal, which depends upon the scattering density difference between the protein and solution (16). HMM scattering intensity profiles in H_2O and D_2O solutions were comparable, suggesting that HMM shape was not affected by the presence of D_2O . For solutions containing divalent ions, 2 mM MgCl_2 or 2 mM CaCl_2 was added to achieve ~ 1 mM free Mg^{2+} or Ca^{2+} . After dialysis, HMM samples were clarified by ultracentrifugation ($150,000 \times g$, 45 min) and concentrated (3–30 mg/ml) using Centricon concentrators (Amicon). Concentration of HMM was estimated assuming 350 kDa for molecular mass and $E_{280 \text{ nm}} = 6.47 \text{ cm}^{-1}$ (15).

Sedimentation Velocity—Sedimentation velocity values for HMM were determined by sucrose density gradient ultracentrifugation as described (17). Thyroglobulin, catalase, aldolase, and albumin (Amersham Biosciences) were used as standards. 100 μg HMM or standard was layered onto a linear 5–20% (w/v) sucrose gradient in buffer containing 150 mM KCl, 20 mM imidazole, pH 7.0, 1 mM EDTA, 1 mM dithiothreitol, and 2 mM MgCl_2 . Samples were centrifuged at 50,000 rpm for 90 min at 10 °C in a 65.1 VTi rotor. 0.5-ml fractions were collected, sucrose concentrations were measured, and proteins were analyzed by SDS-PAGE.

Stokes Radius—The Stokes radius of HMM was determined by gel filtration chromatography using a Superose 6 fast protein liquid chromatography column and protein standards (albumin, catalase, ferritin, thyroglobulin, and laminin). HMM and standards were chromatographed in a solution containing 150 mM KCl, 20 mM imidazole, pH 7.0, 1 mM EDTA, 1 mM dithiothreitol, and 2 mM MgCl_2 .

Molecular weight was determined using the equation (18),

$$M_r = (6\pi\eta NR_s)/(1 - \nu\rho_{20,w}) \quad (\text{Eq. 1})$$

where $\eta = 0.010019 \text{ g/s}\cdot\text{cm}$, $N = 6.02 \times 10^{23}$, R_s represents the Stokes radius (cm), s represents the sedimentation coefficient (Svedberg), ν represents partial specific volume (g/ml), and $\rho_{20,w} = 0.99823 \text{ g/ml}$.

X-ray Scattering Measurements—Small-angle x-ray scattering experiments were performed on the 2-m instrument at Los Alamos National Laboratory (19). The instrument uses a sealed x-ray tube to produce Cu-K_α x-rays (1.54 Å, 8.5 keV) focused to a vertical line at the plane of a one-dimensional position-sensitive detector. Sample and buffer data were collected to produce intensity profiles $I(q)$ versus q ($q = 4\pi(\sin\theta)/\lambda$, λ = wavelength, 2θ = scattering angle) by following published procedures (19). The q range used for data analysis was 0.01–0.15 \AA^{-1} . Data collection times were typically 1–4 h, depending on the sample concentration, and the sample cell was maintained at a constant temperature (7 ± 1 °C) over the course of an experiment. To assess concentration dependence of scattering, scattering data were collected on a dilution series for each HMM protein sample and extrapolated at infinite dilution. Molecular weight, M_r , was calculated by comparing the forward scattering (I_0) at infinite dilution to that of a standard of known molecular weight according to the following equation.

$$M_{r,\text{unknown}} = (I_{0,\text{unknown}}/I_{0,\text{known}}) M_{r,\text{known}} \quad (\text{Eq. 2})$$

Lysozyme ($M_r = 14.2$ kDa, Sigma) (20) was used as the protein standard.

Neutron Scattering Measurements—Neutron scattering data were collected on the NG3 30-m SANS instrument at the National Institute

of Standards and Technology in Gaithersburg, MD. Data were reduced according to published methods (21) to correct for detector sensitivity and sample background. The neutron wavelength was set to 5.5 Å with a wavelength spread $\Delta\lambda/\lambda$ of 0.35 to maximize neutron flux. Sample-to-detector distances of 13.1 and 1.7 m were used to cover the appropriate q -range (0.003–0.025 and 0.021–0.27 \AA^{-1} , respectively). Intensity profiles for samples and corresponding buffers were collected at both detector distances to correct for background. HMM samples (8–10 mg/ml) and buffers were maintained at 10 °C throughout data collection. Typical data collection times were 4 h for the 13.1-m sample-to-detector distance and 30 min for the 1.7-m distance. The data from the two detector distances were merged using procedures included with the National Institute of Standards and Technology data reduction software. The higher contrast and lower measured minimum q value for the neutron scattering experiments meant that these data have significantly greater statistical precision and are able to more accurately determine the scale parameters of the large HMM molecule. Therefore, neutron scattering data were used for all model comparisons.

Small-angle Scattering Data Analysis—The small-angle x-ray or neutron scattering from a homogeneous solution of monodisperse particles can be written as,

$$I(q) = \left\langle \left| \int_V (\rho(\mathbf{r}) - \rho_s) e^{-i\mathbf{q}\cdot\mathbf{r}} d^3r \right|^2 \right\rangle \quad (\text{Eq. 3})$$

where $\rho(\mathbf{r})$ is the scattering length density of the scattering particle and ρ_s is the scattering length density of the solvent. \mathbf{q} is the momentum transfer, having the magnitude given above. The integration over the particle volume is rotationally averaged, and the experiment measures the time and ensemble average for all particles in solution.

In addition to traditional Guinier analysis (22) of the data for the radius of gyration, R_g , the probable distribution of vector lengths within the scattering object, $P(r)$, can be determined from the scattering intensity profile. $I(q)$ and $P(r)$ are related by the Fourier transform in Equation 4.

$$I(q) = 4\pi \int_0^\infty dr \cdot P(r) (\sin(qr))/qr \quad (\text{Eq. 4})$$

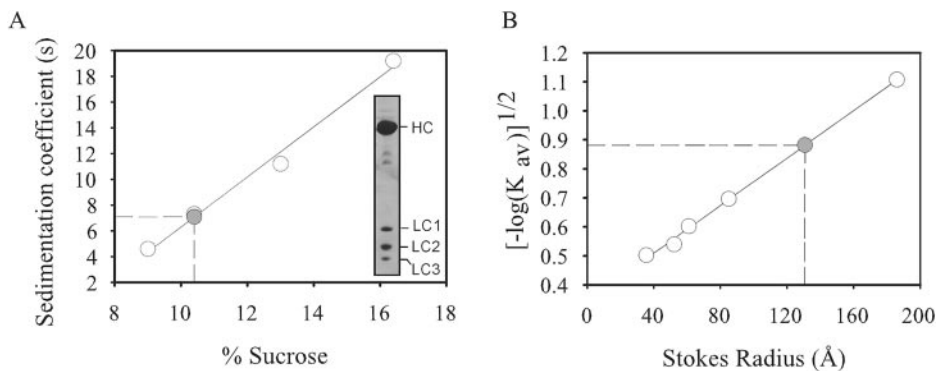
The 0th and second moments of $P(r)$ gives the forward scatter (I_0) and R_g values for the scattering object typically with greater precision than Guinier analysis because the calculations utilize the information in the entire measured scattering profile. The indirect Fourier transform algorithm implemented in the program GNOM (23, 24) was used to determine $P(r)$ from the measured intensity (25, 26). A slit smearing correction was applied to the small-angle x-ray scattering data to correct for the instrument geometry. No correction for smearing was required for the neutron scattering data because the dimensions of the beam are adequately approximated as a point source for these experiments.

Computer Modeling—To compare experimental scattering spectra with a published model of HMM structure (13), simulated scattering intensity profiles and $P(r)$ functions were generated from the atomic coordinates of the model using software (PR_PDB) developed at Los Alamos National Laboratory (27). A second program developed at Los Alamos National Laboratory, called XTAL_STR (28), was used to produce composite models that fit the scattering intensity profiles. The known structures can either be atomic coordinates, such as crystal structure coordinates or coordinates of points randomly distributed within the volume of a shape such as an ellipsoid. Composite model structures are made by randomly positioning and orienting the known structures with respect to one another. The program assumes that the density of each component structure is uniform to calculate $P(r)$ from the coordinates of the substructures. $P(r)$ is transformed into $I(q)$ through the transform defined in Equation 4. The quality of the fit of the model intensity profile to the experimental intensity profile is measured using F , a modification of the reduced χ -squared parameter, as defined in Equation 5.

$$F = \frac{1}{N_{\text{pts}}} \left(\sum_{N_{\text{pts}}} \frac{(I(q) - I_m(q))^2}{\sigma(q)^2} \right) \quad (\text{Eq. 5})$$

N_{pts} is the number of points in the data set, $I(q)$ and $I_m(q)$ are the experimental and model intensity values, respectively, and $\sigma(q)$ is the

FIG. 1. **Physical characteristics of purified HMM.** A, sedimentation coefficient for HMM (7.07 s) determined by sucrose gradient ultracentrifugation. Standards were thyroglobulin (19.2 s), catalase (11.2 s), aldolase (7.3 s), and albumin (4.6 s). *Inset*, 12% SDS-PAGE of HMM produced by α -chymotryptic digestion of myosin. Labels indicate the positions of HMM heavy chain (HC) and myosin light chains (LC_1 , LC_2 , and LC_3). B, determination of Stokes radius of HMM (130 Å) by gel filtration chromatography on a Superose 6 column. Standards were albumin (35.5 Å), catalase (52.2 Å), ferritin (61 Å), thyroglobulin (85 Å), and laminin (186 Å).



experimental uncertainty of $I(q)$. The set of known structures used for the modeling were generated from the Offer and Knight HMM model (13). The original model was broken into three sections, the two S1 heads and the coiled-coil tail. To obtain optimized models using the small-angle scattering data, XTAL_STR was used such that the subunits were constrained to remain in contact at fixed points. Model structures were produced by randomly rotating each substructure around the connection points. Thus, there were six degrees of freedom in the modeling done by XTAL_STR (two hinges with three Euler angles each). The published model has a truncated coiled-coil tail; therefore additional models with longer tails ranging from the length of the published structure (~ 180 Å) up to 1500 Å were tested to find the length that best fit the data. The tail length used for the final modeling was ~ 380 Å. Each XTAL_STR run tested in excess of 300,000 model iterations, and a single best fit model was selected from each run. Three independent runs of XTAL_STR were performed to determine the reproducibility of the modeling.

RESULTS

Purified HMM—Fig. 1 shows physical characteristics of purified HMM. In contrast to HMM produced by tryptic digestion, HMM produced by mild α -chymotryptic digestion is relatively homogenous (15). SDS-PAGE analysis (Fig. 1, *inset*) showed that the HMM heavy chain migrated as a high molecular mass band at ~ 140 kDa. All three light chain peptides were also evident as bands at ~ 21 (LC_1), 19 (regulatory light chain), and 16.5 kDa (LC_3). The sedimentation coefficient (Fig. 1A) and Stokes radius (Fig. 1B) of HMM were determined by sucrose gradient ultracentrifugation and gel filtration chromatography, respectively. A calculated value of 371 kDa for the molecular mass of HMM was obtained using sedimentation coefficient and Stokes radius values (see “Materials and Methods”). The value was similar to published values of HMM (15) and is consistent with HMM being monodisperse in solution.

Scattering Measurements—Fig. 2A shows the neutron scattering intensity profiles obtained for HMM in solutions containing EDTA with and without added Ca^{2+} or Mg^{2+} . The merged data sets for each condition extend over the q range 0.004 – 0.24 Å $^{-1}$. Guinier regions for each data set are shown in Fig. 2B. Each shows evidence for two linear regions, the larger slope associated with the R_g value for the overall shape and the lesser slope associated with the head group region. The rollover of the data at the lowest q values is expected for asymmetric, rod-like particles of finite length. Fig. 2C shows the pair-vector distribution functions, $P(r)$ versus r , obtained via Fourier transform of the data using the GNOM software package. The $P(r)$ profile for each data set exhibited two prominent maxima, one at $r = \sim 37$ Å and one at $r = \sim 110$ Å. The peak at $r = 37$ Å is a consistent feature of $P(r)$ profiles derived from solution scattering measurements of myosin S1 subfragments (29, 30) and, therefore, is likely to reflect interatomic vector lengths within the S1 head. The longer vector lengths most likely reflect contributions from both head-head and head-rod scattering vectors (see below). The $P(r)$ functions were similar for all buffers, suggesting that the overall conformation of HMM was

not measurably different in buffers with or without added divalent cations. The length at which the $P(r)$ function goes to zero gives the maximum chord length of the molecule, d_{max} . All three data sets were fit well at a d_{max} of 390–400 Å and radius of gyration (R_g) values of 110–112 Å using neutron scattering data with a q_{min} of 0.004 Å $^{-1}$. A d_{max} value of ~ 400 Å is consistent with electron microscope observations that indicate a sharp bend in the myosin rod 43 nm from the head-tail junction (11). Flexibility of the rod at this position and limitations from q_{min} could contribute to an apparent foreshortening from the longest estimated lengths of the S2 rod (72 nm) (31).

X-ray scattering measurements were used to obtain plots of R_g versus concentration, c , to extrapolate values of R_g at infinite dilution (Fig. 2D). For these data scattering was corrected for effects of slit smearing (see “Materials and Methods”), and R_g values were again determined from $P(r)$ analysis. As expected for monodisperse particles, the R_g versus c relations showed either no concentration dependence or showed that R_g decreased with increasing c , which is characteristic of interparticle interference. The difference between the R_g of HMM in solutions containing EDTA and in solutions containing free added Mg^{2+} or Ca^{2+} is not statistically significant, consistent with our conclusion from the neutron scattering data that the addition of divalent cations does not cause a large scale redistribution of molecular mass, *i.e.* the disposition of the head groups with respect to each other and to the rod are similar for each form.

I_0 values obtained from $P(r)$ analysis of the x-ray scattering data were used to calculate molecular weight values by comparison with lysozyme as a standard (20). Molecular weight values calculated from the x-ray scattering data underestimated published values for chymotryptic HMM by as much as 25%. The underestimate was likely due to the large dimensions of HMM combined with our limited ability to collect x-ray scattering data below 0.01 Å $^{-1}$, which are required to adequately sample the long vector lengths within the particle. Indeed the $P(r)$ profiles calculated from the x-ray scattering data go to zero at shorter vector lengths (~ 270 Å), effectively truncating the vector lengths associated with the long tail of the HMM molecule.

Model Structures—To determine whether the existing model of the head-tail junction of myosin (13) could adequately account for experimental scattering by HMM, neutron scattering profiles were compared with simulated spectra from a similar model. The original model was constructed by aligning the crystal coordinates of two scallop regulatory domains with model coordinates for a scallop α -helical coiled-coil rod. The remainder of the catalytic domain was generated by the addition of chicken S1 coordinates (1). According to the resulting structure, the two S1 heads are predicted to lie in a plane nearly anti-parallel to one another, with heads overlapping at the distal ends of the light chain binding domains. The struc-

FIG. 2. **Small-angle scattering by HMM.** A, basic neutron scattering curves of HMM in experimental buffers. Scattering data were collected at two separate detector distances (13.1 and 1.7 m), background-subtracted, and merged in the region of overlap. Data, reduced to $\log[I(q)]$ versus q , are shown for HMM in solutions containing 1 mM EDTA (closed circles), 1 mM EDTA + 2 mM MgCl_2 (open circles), and 1 mM EDTA + 2 mM CaCl_2 (squares). Data points for the three solutions essentially superimpose; closed circles and square curves were arbitrarily shifted along the vertical axis for clarity. B, Guinier regions for HMM in solutions containing 1 mM EDTA (closed circles), 1 mM EDTA + 2 mM MgCl_2 (open circles), and 1 mM EDTA + 2 mM CaCl_2 (squares). Open circle and open square curves were arbitrarily shifted along the vertical axis for clarity. C, $P(r)$ transformations of the data shown in A obtained using GNOM software. D, concentration dependence of R_g determined from x-ray scattering measurements. R_g values were calculated from scattering data using GNOM software.

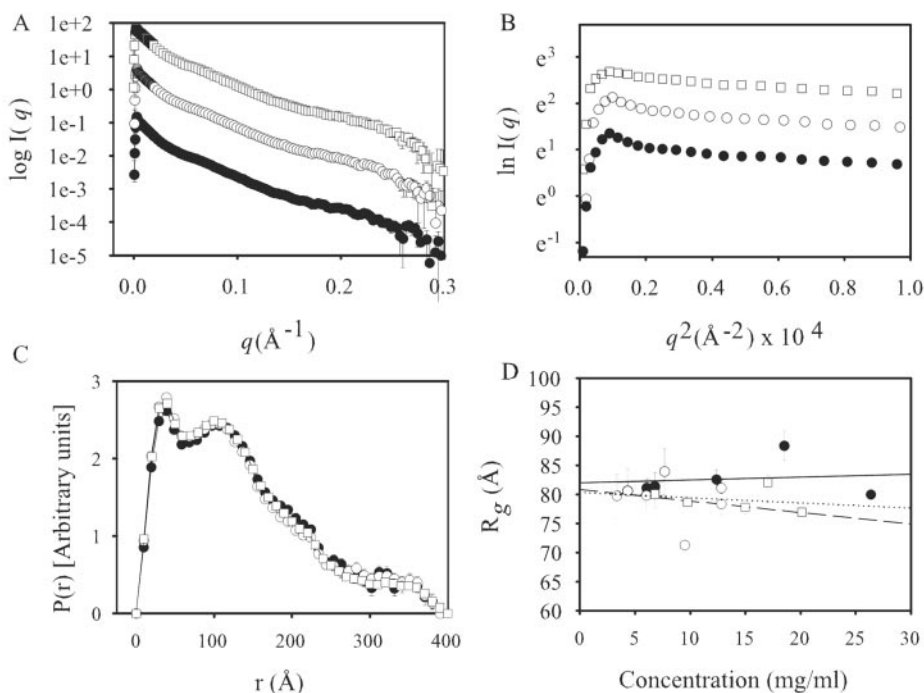


FIG. 3. **Comparison of a theoretical $P(r)$ function calculated from a model HMM structure with that calculated from neutron scattering data.** A, wire-frame model of an HMM model similar to that developed by Offer and Knight (13). B, comparison of simulated $P(r)$ functions (gray) from the model shown in A with $P(r)$ data of HMM in buffers containing EDTA (black). $P(r)$ functions are shown on a relative scale such that the area under each curve is proportional to the molecular weight of the scattering particle.

ture has 2-fold rotational symmetry about the axis of the coiled-coil tail.

Scattering intensity profiles were generated from the model using an algorithm previously described (27). Intensity profiles were also generated from models with coiled-coil tails of varying lengths (see “Materials and Methods”). Fig. 3A shows one such model (tail length = 380 Å) and a comparison of $P(r)$ functions (Fig. 3B) derived from the model to that obtained from experimental scattering data (neutron scattering data from HMM in solutions containing EDTA). Although the maxima at $r = \sim 37$ and 110 Å in the experimental $P(r)$ were reproduced reasonably well by the simulated data, the relative intensities of the two peaks differed between the experimental and model $P(r)$ functions. The functions also differed at a third maximum ($r = \sim 200$ Å), with the model $P(r)$ function giving a much more pronounced peak compared with the experimental data function. The comparisons indicate that significant differences exist between the published HMM model (13) and HMM conformation in solution.

Three independent best-fit models produced by allowing the two S1 heads to freely rotate relative to the S2 tail are shown in Fig. 4. As can be seen from the wire frame models, all three of the structures obtained using this approach exhibited similar features, although two of the models differed from the third with respect to chirality (handedness) of the heads. Because small-angle scattering cannot distinguish between equivalent conformations of different handedness, neither conformation

can be excluded. Compared with the starting model (Fig. 3A), the S1 heads in the optimized models are less planar and show marked asymmetry with respect to the rod. Fig. 5 shows the $P(r)$ functions of the models compared with that derived from experimental neutron scattering data. All three models reproduce the initial peak at $r = \sim 37$ Å and approximate the relative intensity of a second maximum. However, the position of the second maximum shifts to shorter vector lengths ($r = \sim 87$ versus 110 Å). A third peak at $r = \sim 176$ Å is also more prominent in the model $P(r)$ functions.

$P(r)$ functions derived from the breakdown of one of the models produced by XTAL_STR into its component parts are shown in Fig. 6. According to this analysis, the three broad maxima in the $P(r)$ profile of the complete model can be deconstructed into four peaks arising from model subcomponents. The first and second of these, occurring at $r = 37$ and 85 Å, are due primarily to scattering lengths within the individual heads and between the individual heads and the rod, respectively. The third and fourth, at $r = 115$ and 176 Å, are due to vectors corresponding to distances between the two S1 heads. Potentially, the ratio of the first and second peak intensities could be affected by segmental flexibility of the rod and account for divergence of vector lengths among model and experimental data in this region. Similarly, flexion of the individual heads at the junction between the catalytic and light chain binding domains (29) could modulate peak intensity at $r = 176$ Å. However, these additional points of flexibility were not incor-

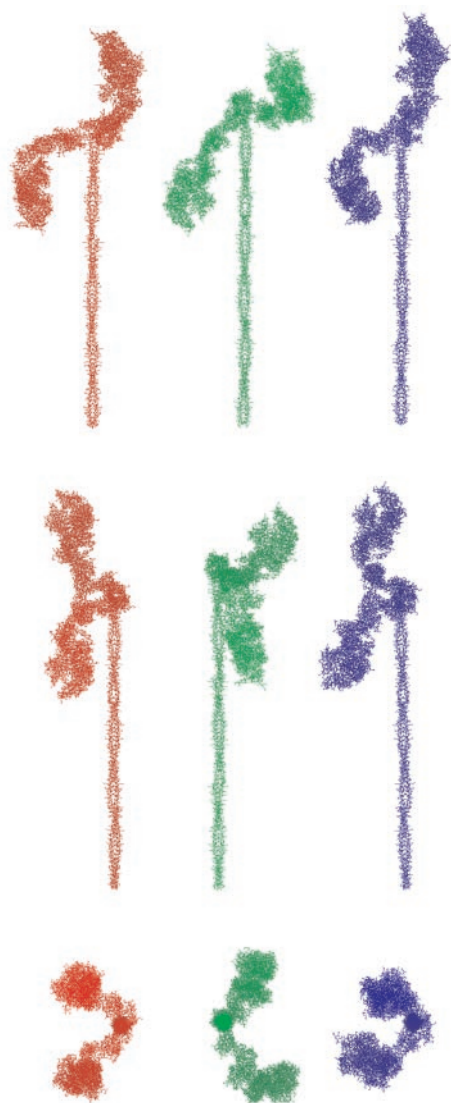


FIG. 4. **Wire-frame representations of three best-fit HMM structural models.** *Top*, longitudinal view. *Middle*, view as in *top panels* but rotated $\sim 90^\circ$ counterclockwise. *Bottom*, view down rod axis. Model 1011 (red), $F = 1.98$; Model 1508 (green), $F = 2.09$; Model 1608 (blue), $F = 2.16$.

porated into the current modeling because they would have introduced an unacceptable number of degrees of freedom into the modeling.

DISCUSSION

The results presented here are the first to use small-angle x-ray and neutron scattering measurements to produce a model of the three-dimensional structure of a double-headed myosin fragment in solution. In contrast to previous studies of HMM by small-angle x-ray scattering (32, 33), we utilized available S1 crystal structures to construct HMM models that satisfy experimental scattering profiles of HMM in solution. Although equivalent small-angle scattering intensity profiles do not necessarily imply a unique structural solution, the ability to obtain reproducible fits using constraints of known crystal structures suggests that the models described here are reasonable representations of the three-dimensional shape of two-headed myosin in solution. The major new finding of this work is that the head-tail junction of HMM is not symmetric.

Although it has been appreciated that the two heads of myosin may adopt defined conformations with respect to one another, especially within the thick filament (34–39), and that

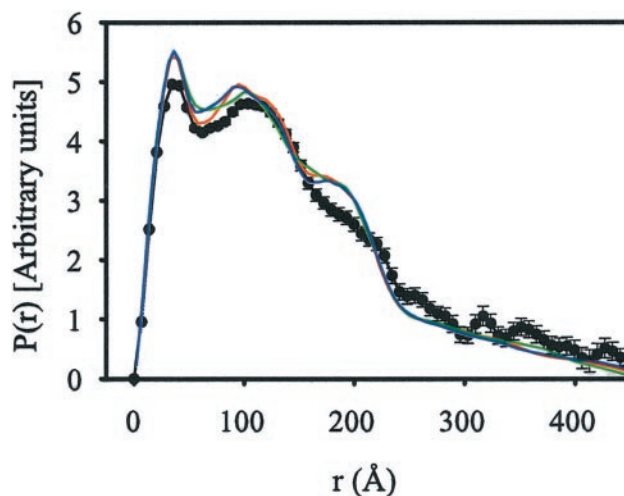


FIG. 5. **Comparison of theoretical $P(r)$ functions calculated from best-fit HMM structural models using PR_PDB.** Neutron scattering data is shown in black, model 1011 is shown in red, model 1508 is shown in green, and model 1608 is shown in blue. $P(r)$ functions were generated from the scattering data using GNOM software, and the area under each curve was normalized to 1.

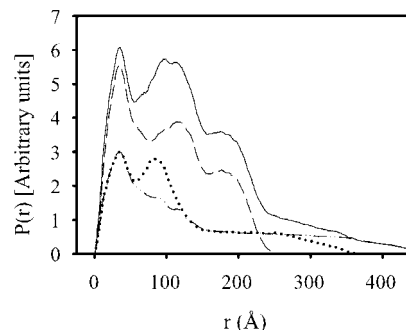


FIG. 6. **$P(r)$ functions derived from component parts of Model 1011.** Solid line, complete model; dashed line, up head and down head; dotted line, down head and rod; dashed and dotted line, up head and rod.

such relationships are likely to have regulatory significance (40, 41), it has proven difficult to define those interactions in isolated myosin. For instance, most electron micrographs of myosin or HMM show that the heads adopt random angles with respect to one another and to the rod (11, 42, 43). These and other data suggest that both the S1-S2 junction and the junction between the catalytic and regulatory domains of S1 are points of flexibility in myosin (44). On the other hand, the notion that the two heads of myosin adopt conformations independent of one another was recently called into question by a model reconstruction of the head-tail junction of myosin (13). The model was constructed by docking a crystal structure of the scallop regulatory domain (2) to that of a scallop coiled-coil helix. Assumptions made in docking the structures were that the WP helix (*i.e.* the “hook” helix) of the scallop regulatory domain was continuous with the α -helix of the coiled-coil tail and that the entire repeating heptad sequence of the tail forms a helical coiled-coil. According to the resulting model the two S1 heads were predicted to emerge at angles tangential to the myosin tail, lie anti-parallel to one another, and be related to each other by a 2-fold axis of symmetry. Furthermore, based on steric considerations and the results of molecular dynamics simulations, the positions of the two heads relative to one another were predicted to be relatively static (13).

Our current results demonstrate that simulated scattering from an HMM model comparable with that of the head-tail

junction of scallop HMM (13) does not reproduce scattering by HMM in solution. In particular, the third maximum $P(r)$ function of the model was not present in the $P(r)$ function calculated from the data. Calculation of the $P(r)$ functions for model sub-components show that this third maximum is related to the position of the heads relative to one another. The results indicate that the average relationship of the two S1 heads differs from that predicted by the model of the scallop head-tail junction (13).

Several explanations for the difference between experimental and predicted observations are possible. First, the original model was based on a chimeric HMM molecule composed of crystal structures from both scallop and chicken S1 domains, whereas our experimental scattering was obtained from purified rabbit fast skeletal HMM. Although it may be reasonable to expect that scattering from the chimeric HMM (probably closest to scallop HMM in the "on" state) might resemble vertebrate striated HMM, this is not necessarily the case. Second, conditions under which the experimental scattering data were collected may also influence the conformation of the heads relative to each other. The presence or absence of divalent cations did not appear to affect scattering intensity profiles in the current study. However, temperature (40), ionic strength (45), and the absence of added nucleotides (29, 46) may still affect HMM conformation and could account for differences between the experimental and model scattering. Alternatively, differences between the experimental and predicted HMM scattering profiles may be indicative of systematic differences between model predictions of the head-tail junction and the actual disposition of myosin heads in solution. In this case, the XTAL_STR models obtained by allowing the S1 heads to rotate relative to one another and the rod may be more representative of the average shape of HMM in solution.

Characteristics of the optimized models that distinguish them from the original representation of the myosin head-tail junction include a marked departure from symmetry, a tendency for the light chain binding domains to be related by angles of less than 180° (as opposed to anti-parallel), and a tendency for one of the two S1 heads to be bent back toward the S2 rod. Although these properties clearly differentiate the optimized models from the starting model, they agree well with electron micrograph representations of HMM (11, 42, 43). The lack of symmetry between the heads is also consistent with findings from 2-dimensional cryoelectron projections of smooth muscle HMM in both the thiophosphorylated ("on") and unphosphorylated ("off") states (5, 47). Although it could be argued that asymmetry in the latter models was artificially imposed by the packing of HMM molecules into a two-dimensional lattice, our results indicate that S1 head asymmetry persists even in solution.

The notion that the myosin heads exhibit structural and functional asymmetry due to steric constraints within the thick filament or upon actin binding has been suggested (37–39). For instance, although it is well established that each S1 head of myosin, when isolated by proteolytic digestion, is functionally identical to the other head with respect to ATPase activity and nucleotide and actin binding affinities, it seems likely that some nonequivalent behavior is induced by actin binding. This is because in order for both heads to bind to actin in the same filament either unwinding of a portion of the rod is necessary or distortion of the second S1 head is required (7). Cooperative or ordered binding may result (8) and could potentially explain the greater force and displacement observed for HMM compared with S1 in single molecule experiments (9).

Whereas asymmetry due to steric considerations may be imposed on the myosin molecule, the present results suggest

that differences in the orientations of the two S1 heads are intrinsic to the structure of the myosin dimer (48). At present, however, the molecular basis for asymmetry between heads is speculative since the positions of the pivot points linking the S1 heads to the tail were arbitrarily chosen for the current modeling. Nonetheless, by combining molecular dynamics simulations with the model of the scallop head-tail junction, Offer and Knight (13) identified three points of flexibility within the molecule, two within the long α -helix of the S1 regulatory domain and one in the coiled-coil tail, which allow the two heads to move with respect to the tail. Potentially, flexion at any of these points could contribute to the overall disposition of myosin heads in solution. Alternatively, flexibility at the WXW motif, which confers the sharp bend near the end of S1 regulatory domain (1) or unwinding of the coiled-coil tail near the invariant proline (12, 49), could also account for asymmetric head position.

In summary, we used small-angle scattering to investigate the three-dimensional shape of HMM in solution. Comparison of the experimental scattering profiles to models of the head-tail junction of HMM showed that the scattering profiles were most closely fit by models in which the positions of the two S1 heads were nonequivalent and asymmetric. It will be of interest to determine whether the disposition of the S1 heads in HMM is affected by the presence of added nucleotides or nucleotide analogues. If so, small-angle scattering techniques combined with high resolution models of HMM will continue to prove valuable for understanding interactions and contributions of both S1 heads during the catalytic cycle of myosin.

Acknowledgments—We thank Dr. Gerald Offer for kindly providing the structural coordinates of the scallop head-tail junction model and Drs. James Ervasti and Inna Rybakova for technical assistance with sucrose gradient assays. We also thank Chad Warren and Cinder L. Krema for assistance in the purification of HMM and Brian Macdonald for technical assistance with small-angle x-ray scattering measurements. Neutron scattering data were obtained using instrumentation supported by the National Science Foundation under agreement DMR-9423101 at the Cold Neutron Research Facility at the National Institute of Standards and Technology.

REFERENCES

1. Rayment, I., Rypniewski, W. R., Schmidt-Base, K., Smith, R., Tomchick, D. R., Benning, M. M., Winkelmann, D. A., Wesenberg, G., and Holden, H. H. (1993) *Science* **261**, 50–58
2. Xie, X., Harrison, D. H., Schlichting, I., Sweet, R. M., Kalabokis, V. N., Szent-Gyorgyi, A. G., and Cohen, C. (1994) *Nature* **368**, 306–312
3. Dominguez, R., Freyzon, Y., Trybus, K. M., and Cohen, C. (1998) *Cell* **94**, 559–571
4. Holmes, K. C. (1997) *Curr. Biol.* **7**, 112–118
5. Wendt, T., Taylor, D., Messier, T., Trybus, K. M., and Taylor, K. A. (1999) *J. Cell Biol.* **147**, 1385–1389
6. Metzger, J. M., Greaser, M. L., and Moss, R. L. (1989) *J. Gen. Physiol.* **93**, 855–883
7. Offer, G., and Elliott, A. (1978) *Nature* **271**, 325–329
8. Conibear, P. B., and Geeves, M. A. (1998) *Biophys. J.* **75**, 926–937
9. Tyska, M. J., D. E., D., Guilford, W. H., Patlak, J. B., Waller, G. S., Trybus, K. M., Warshaw, D. M., and Lowey, S. (1999) *Proc. Natl. Acad. Sci. U. S. A.* **96**, 4402–4407
10. Mendelson, R. A., Morales, M. F., and Botts, J. (1973) *Biochemistry* **12**, 2250–2255
11. Elliott, A., and Offer, G. (1978) *J. Mol. Biol.* **123**, 505–519
12. Knight, P. J. (1996) *J. Mol. Biol.* **255**, 269–274
13. Offer, G., and Knight, P. (1996) *J. Mol. Biol.* **256**, 407–416
14. Wagner, P. D., and Giniger, E. (1981) *J. Biol. Chem.* **256**, 12647–12650
15. Weeds, A. G., and Pope, B. (1977) *J. Mol. Biol.* **111**, 129–157
16. Wall, M. E., Gallagher, S. C., and Trehwella, J. (2000) *Annu. Rev. Phys. Chem.* **51**, 355–380
17. Amann, K. J., Guo, A. W., and Ervasti, J. M. (1999) *J. Biol. Chem.* **274**, 35375–35380
18. Siegel, L. M., and Monty, K. J. (1966) *Biochim. Biophys. Acta* **112**, 346–362
19. Heidorn, D. B., and Trehwella, J. (1988) *Biochemistry* **27**, 909–915
20. Krigbaum, W. R., and Kugler, F. R. (1970) *Biochemistry* **9**, 1216–1223
21. Hammouda, B., Barker, J. G., and Krueger, S. (1996) *Small Angle Neutron Scattering Manuals*, National Institute of Standards and Technology, Gaithersburg, MD
22. Guinier, A. (1939) *Ann. Phys. (Paris)* **12**, 161–237
23. Svergun, D. (1991) *J. Appl. Crystallogr.* **24**, 485–492
24. Svergun, D. (1992) *J. Appl. Crystallogr.* **25**, 495–503
25. Svergun, D. I., and Semeniuk, A. V. (1987) *Dokl. Akad. Nauk SSSR* **297**,

- 1373–1377
26. Svergun, D. I., Semeniuk, A. V., and Feigin, L. A. (1988) *Acta Crystallogr. Sect. A* **44**, 244–250
27. Gallagher, S. C., Callaghan, A. J., Zhao, J., Dalton, H., and Trehwella, J. (1999) *Biochemistry* **38**, 6752–6760
28. Heller, W. T., Abusamhadneh, E., Finley, N., Rosevear, P. R., and Trehwella, J. (2002) *Biochemistry* **41**, 15654–15663
29. Wakabayashi, K., Tokunaga, M., Kohno, I., Sugimoto, Y., Hamanaka, T., Takezawa, Y., Wakabayashi, T., and Amemiya, Y. (1992) *Science* **258**, 443–447
30. Garrigos, M., Mallam, S., Vachette, P., and Bordas, J. (1992) *Biophys. J.* **63**, 1462–1470
31. Lu, R. C. (1980) *Proc. Natl. Acad. Sci. U. S. A.* **77**, 2010–2013
32. Mendelson, R. A., and Wagner, P. D. (1984) *J. Mol. Biol.* **177**, 153–171
33. Faruqi, A. R., Cross, R. A., and Kendrick-Jones, J. (1991) *J. Cell Sci. Suppl.* **14**, 23–26
34. Squire, J., Cantino, M., Chew, M., Denny, R., Harford, J., Hudson, L., and Luther, P. (1998) *J. Struct. Biol.* **122**, 128–138
35. Padron, R., Alamo, L., Murgich, J., and Craig, R. (1998) *J. Mol. Biol.* **275**, 35–41
36. Taylor, K. A., Reedy, M. C., Reedy, M. K., and Crowther, R. A. (1993) *J. Mol. Biol.* **233**, 86–108
37. Gu, J., Xu, S., and Yu, L. C. (2002) *Biophys. J.* **82**, 2123–2133
38. Juanhuix, J., Bordas, J., Campmany, J., Svensson, A., Bassford, M. L., and Narayanan, T. (2001) *Biophys. J.* **80**, 1429–1441
39. Linari, M., Lucii, L., Reconditi, M., Casoni, M. E., Amenitsch, H., Bernstorff, S., Piazzesi, G., and Lombardi, V. (2000) *J. Physiol. (Lond.)* **526**, 589–596
40. Xu, S., Gu, J., Rhodes, T., Belknap, B., Rosenbaum, G., Offer, G., White, H., and Yu, L. C. (1999) *Biophys. J.* **77**, 2665–2676
41. Levine, R., Weisberg, A., Kulikovskaya, I., McClellan, G., and Winegrad, S. (2001) *Biophys. J.* **81**, 1070–1082
42. Slayter, H. S., and Lowey, S. (1967) *Proc. Natl. Acad. Sci. U. S. A.* **58**, 1611–1618
43. Knight, P., and Trinick, J. (1984) *J. Mol. Biol.* **177**, 461–482
44. Burgess, S. A., Walker, M. L., White, H. D., and Trinick, J. (1997) *J. Cell Biol.* **139**, 675–681
45. Frado, L. Y., and Craig, R. (1992) *J. Muscle Res. Cell Motil.* **13**, 436–446
46. Katayama, E., Ohmori, G., and Bab, N. (1998) in *Mechanisms of Work Production and Work Absorption in Muscle* (Sugi and Pollack, eds) pp. 37–45, Plenum Press, New York
47. Wendt, T., Taylor, D., Trybus, K. M., and Taylor, K. (2001) *Proc. Natl. Acad. Sci. U. S. A.* **98**, 4361–4366
48. Schaub, M. C., and Watterson, J. G. (1981) *Biochimie (Paris)* **63**, 291–299
49. Rimm, D. L., Sinard, J. H., and Pollard, T. D. (1989) *J. Cell Biol.* **108**, 1783–1789